Multianalytical Study of Historical Luminescent Lithopone for the Detection of Impurities and Trace Metal Ions

Sara Bellei,*[,†,‡] Austin Nevin,[†] Anna Cesaratto,[‡,∥] Valentina Capogrosso,[‡] Hervé Vezin,[§] Caroline Tokarski,[⊥] Gianluca Valentini,[‡] and Daniela Comelli[‡]

[†]Istituto di Fotonica e Nanotecnologie - Consiglio Nazionale delle Ricerche (CNR-IFN), Piazza Leonardo da Vinci 32, Milano, 20133 Italy

[‡]Dipartimento di Fisica, Politecnico di Milano, Piazza Leonardo da Vinci 32, Milano, 20133 Italy

[§]Laboratoire de Spectrochimie Infrarouge et Raman (LASIR), UMR CNRS 8516, Université de Lille 1 Sciences et Technologies, 59655 Villeneuve d'Ascq Cedex, France

[⊥]Miniaturisation pour la Synthèse, l'Analyse & la Protéomique (MSAP), USR CNRS 3290, Université de Lille 1 Sciences et Technologies, 59655 Villeneuve d'Ascq Cedex, France

Received: February 10, 2015
Accepted: May 15, 2015

Lithopone is a modern inorganic white pigment composed of a coprecipitate of zinc sulfide (ZnS) and barium sulfate ($BaSO_4$). It was manufactured on a commercial scale starting in 1874 and sold under different names (Griffith white, Charlton White, Orr's Zinc White). It found its application first in the cheaper grades of polish varnishes, floor paints, and paints for interiors as a substitute of lead white. Despite the cheapness of its manufacturing processes and good property as pigment, lithopone had the tendency to darken when exposed to sunlight.[1] To prevent discoloration, starting in 1928, a small amount of cobalt, varying from 0.02% to 0.5% of the zinc content, was added prior to the calcination process.[2] Nevertheless, due to the photodarkening effect, lithopone earned a bad reputation that made its usage as an artists' pigment difficult to establish.[3] Lithopone was likely used as a cheap extender for other white pigments like ZnO or sold under ambiguous names and then involuntarily used by artists. Lithopone as a pigment can be still purchased today.

The identification of lithopone is not straightforward with elemental analysis such as X-ray fluorescence (XRF), since data does not permit the distinction between lithopone from mixtures of barium sulfate and zinc sulfide or zinc oxide present as unprecipitated compounds. A noninvasive protocol for identification of the pigment has been proposed with the aid of different molecular spectroscopy techniques, such as fiber-optic reflectance spectroscopy (FORS) in the UV-vis-NIR and micro-Raman analyses.[4] Few studies have dealt with the photoluminescence (PL) properties of lithopone: in 2012, Comelli et al.[5] published results of PL attributed to Zn-based whites in a painting by *Vincent Van Gogh "Les bretonnes et le pardon de Pont Aven"* (Milan, Galleria di Arte Moderna). In 2014, Capua[3] attributed a green phosphorescent emission on some watercolors by American artist *John La Farge* to lithopone.

The PL properties of lithopone depend essentially on those of ZnS. ZnS is a II−VI compound semiconductor with two main crystalline forms: the more stable cubic form (zinc blende or sphalerite) and the hexagonal form (wurtzite), which is formed after treatment at high temperature.[6] The semiconductor has a direct band gap of 3.54 eV (cubic) or 3.91 eV (hexagonal) at room temperature. After annealing, pure ZnS shows an emission band in the blue region, with an emission

Table 1. List of Samples Analyzed as Part of This Study with Historical Information Regarding Their Manufacture

sample name	pigment name	manufacturer	geographical location	manufacturing period
commercial_ZnS	--	Kremer Pigmente GmbH&Co	Germany	commercially available
commercial_lithopone	--	Kremer Pigmente GmbH&Co	Germany	commercially available
S1	unknown	New Jersey Zinc Company (now HorseHead Corporation)	New Jersey, USA	1848−1966
S2	unknown	Acme	unknown	>1922
S3	unknown	DuPont	Delaware, USA	>1922
S4	unknown	The Chemical	unknown	unknown
S5	Ponolith	Krebs Pigment and Chemical Company (now DuPont)	Delaware, USA	1902−1929
S6	Ponolith	Krebs Pigment and Chemical Company (now DuPont)	Delaware, USA	1902−1929

maximum ranging from 416 to 478 nm assigned to vacancies or interstitial defects in ZnS.[7,8] The addition of a few ppm of a suitable activator into the ZnS matrix creates an efficient light-emitting material, which has been exploited both in bulk material and in nanocrystalline form. In doped ZnS, recombination occurs via shallow trap states or via deep trap states of different kinds which are created by the interaction of the doping element with the semiconductor matrix. Most common activators for phosphorescent ZnS are Mn,[9−11] Cu,[10−13] and Ag;[11,14,15] other impurities, including Al[16,17] and Cl ions,[13,17] have also been investigated. Thus, it has been hypothesized that historical lithopone pigments, which were produced using nonperfect synthesis processes, can be associated with metal impurities which can act as luminescent centers.

In this work, we aim to provide new insights into the optical properties of historical lithopone samples through the combination of spectrally- and time-resolved PL imaging, for the quick identification and mapping of luminescent impurities, and electron paramagnetic resonance (EPR) analysis for the assessment of the presence of specific impurities and defects, which are responsible for the luminous properties of the pigment.

MATERIALS AND METHODS

Six historical samples (S1−6) of lithopone from the beginning of the 20th Century, synthesized in the United States of America, have been investigated. Samples come from the Chamot-Cornell collection and were provided by Joseph Barabe, McCrone Pigments. In Table 1, a list of samples with the indication of the manufacturers is provided. One commercial sample of lithopone and one of ZnS (Kremer Pigmente GmbH&Co., Germany) were studied for comparison.

Powder from each sample was divided into three portions. The first part was used for bulk analysis; the second portion was adequately dispersed between two layers of UV-transparent silica glass of approximately 40 μm thickness to perform PL microscopy, and the third part was used for EPR analysis. For EPR analysis, each sample powder was placed in a thin-walled quartz sample tube with inner dimensions of 1 mm.

System Setup. *X-ray Fluorescence (XRF).* XRF analysis was performed with a portable EDXRF spectrometer (Elio Spectrometer, XGlab srl, Milan, Italy).[18] The instrument can detect elements from Na to U, with a field of analysis between 1 and 40 keV.

Raman Analysis. Raman analysis was performed using a portable Raman spectrometer,[19] based on a 785 nm semiconductor laser (Lion, Sacher Lasertechnik GmbH, Germany) with adjustable power from 0 to 280 mW. A spectrometer (SpectraPro2150, Princeton Instruments, USA) equipped with a 1200 grooves/mm grating and coupled to a front illuminated cooled CCD (PIXIS 100, Princeton Instruments, USA) is employed for spectra registration, covering a spectral range of 150−1200 cm^{-1} at a resolution of approximately 15 cm^{-1}. Through fiber optics, the laser and the spectrometer are connected to a properly designed microprobe, working in backscattering geometry and focusing laser light in a 100 μm (diameter) spot. Density power on samples has always been kept below 500 W/cm^2.

Scanning Electron Microscopy (SEM). Morphologies and the microstructure of samples were imaged with a scanning electron microscope (SEM, Zeiss EVO 50 EP). Powders were deposited on a carbon tape suitable for SEM analyses and sputter-coated with a 10 nm layer of gold.

Multispectral PL Microscopy. Multispectral PL microscopy was performed with an optical microscope (Leica DM RE) equipped for epi-fluorescence measurements. Emission was excited by the 365 nm line of a mercury lamp with the aid of a microscope cube mounting proper excitation and dichroic filters (ET365/10 and ZT390dclp, Chroma Technology Corporation.). Seven band-pass transmission filters from 400 to 700 nm with a spectral band of 40 nm (FKB-VIS-40, Thorlabs Inc.) were used to measure a selected part of the emission spectrum. The image detector employed was a low-noise monochrome CCD camera (Retiga 2000R, QImaging, Canada). Images were typically acquired using 20× or 50× objectives, with a resulting sampling pitch of 1.8 and 0.7 μm, respectively, due to the camera pixel size. A sequence of seven spectral images between 400 and 700 nm in steps was acquired by changing the filter manually. Assuming the spectral transmission of each filter as a Dirac delta function peaked on the central wavelength and following proper correction for the detector efficiency, emission spectra at all points of the field of view were reconstructed. The color image of the emission, calculated on the basis of the RGB color space, was employed as a rapid indication of the emission in the analyzed area.

Time-Resolved PL Microscopy. Time-resolved measurements have been performed on the same microscope but exciting emission through a Q-switching frequency-tripled diode-pumped Nd:YAG laser (FTSS 355-50 Crylas GmbH, Berlin, Germany, λ = 355 nm, Pulse energy = 70 μJ, pulse duration = 1.0 ns). The laser beam is coupled to a 600 μm silica optical fiber and projected onto the object plan through a proper optical system composed of three plano-convex lenses (focal length = 10, 100, and 50 mm) in order to uniformly illuminate the field of view. The dynamics of the emission is detected by a gated intensified CCD camera (C9546-03, Hamamatsu Photonics, 100 ns gate width, temporal jitter ∼0.1 ns) based on a GaAs photocathode with spectral sensitivity from 380 to 850 nm. Spatial resolution essentially depends on that of the intensifier (57 lp/mm), resulting in a value of 1.5

μm when employing the 50× objective. For data analysis, luminescence lifetime maps have been produced by modeling data with a monoexponential decay, providing a qualitative estimation of the heterogeneity of the decay kinetic of the emission from samples. Following this, in each lifetime map areas with similar kinetic emissions have been clustered together by employing image segmentation on the basis of k-means clustering. The mean luminescence decay extracted in each cluster has then been fitted on the basis of a multiexponential decay model (with a maximum of three components) as described elsewhere.[5] Multispectral and time-resolved PL measurement have been performed on the same area in order to correlate results.

Electron Paramagnetic Resonance (EPR) Spectroscopy. EPR spectra of all the samples were recorded at room temperature using a Bruker E500 spectrometer operating at X-band frequency of 9 GHz, having a 2 G of amplitude modulation and 5 mW for the microwave power.

RESULTS

Preliminary bulk measurements on historical samples with Raman and XRF spectroscopy confirmed that the pigments contained elemental and molecular signals attributed to lithopone: representative Raman and XRF spectra of sample S2 are shown in Figure 1, with typical Raman shifts of ZnS (348

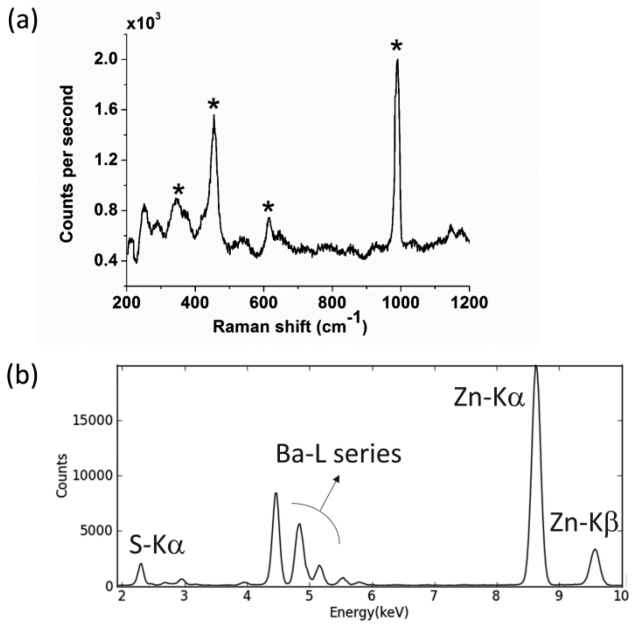

Figure 1. Analysis of Sample 2 with (a) Raman spectroscopy with 785 nm excitation; ZnS (348 cm^{-1}) and $BaSO_4$ (455, 616, and 987 cm^{-1}) Raman bands are marked with asterisks. (b) X-ray fluorescence spectroscopy.

cm^{-1}) and $BaSO_4$ (455 and 987 cm^{-1}) and the presence of Zn, S, and Ba as the main elements. XRF did not detect other trace elements, suggesting that, if metallic impurities are present, their concentration is below the detection limit of the portable XRF analyzer.

SEM images for commercial lithopone and for representative historical samples are shown Figure 2. The intimate mixture of white ($BaSO_4$) and light gray (ZnS) particles demonstrates that coprecipitates of different dimensions have been formed, with the largest particles, on the order of 1 μm in diameter, present

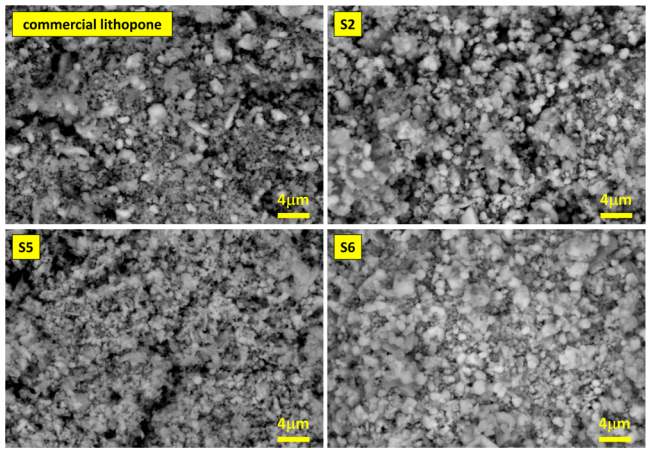

Figure 2. Scanning electron microscope images for commercial lithopone and historical samples S2, S5, and S6. Images highlight the presence of a uniform distribution of particles of ZnS and $BaSO_4$. Differences in particle size are ascribed to grinding grade or thermal treatments during pigment preparation. See Supporting Information for SEM images of other samples.

in samples S1, S3, and S4 (see SEM images of all samples in the Supporting Information). Differences in particle size can be attributed both to a different grinding grade and to effects of thermal treatments, which led to the formation of crystals of different sizes.

Preliminary PL measurements on bulk samples (data not shown) highlighted a noticeable emission from historical samples with a high variability among them, which was better investigated with PL microscopy: from an inspection of the RGB reconstructed maps of the emission (Figure 3), the historical samples have small localized luminescent centers, with a variable diameter of a few micrometers, emitting at different wavelengths, and are distributed over a more uniform and less-intensely emitting matrix. In general, blue (BL, λ = 500 nm), green-yellow (GL, λ = 550 nm), and orange (OL, $\lambda \geq 600$ nm) luminescent centers can be clearly detected. In comparison, both commercial samples of lithopone and ZnS show a less intense emission with only few emitting centers.

Strong variations in historical samples are probably due to differences either in synthesis processes or in ores from which the pigments were produced. According to the color of the emission of the matrix and the distribution of impurities, three classes of lithopone are observed: samples S2 and S3 have strong-emitting luminescent centers mainly with maxima in the blue and in the green-yellow region of the electromagnetic spectrum; samples S1, S4, and S5 are associated with a weakly red-emitting matrix and have small multicolored luminescent centers; sample S6 has a strong blue-emitting matrix and a variety of small emitting centers of different colors. For all samples, we hypothesize that the localized emission centers are metallic impurities in trace concentrations unintentionally introduced into the ZnS crystal lattice during synthesis. The correlation between the wavelength emitted by the emitting center and its nature will be discussed in the following section.

Time-resolved imaging analysis, performed on the same areas observed using multispectral imaging, provided a characterization of their decay kinetics. The decay emission parameters of luminescent centers detectable in four samples (S2, S5, and S6, representing the three classes described above, and S4, characterized by a lower emission intensity) have been

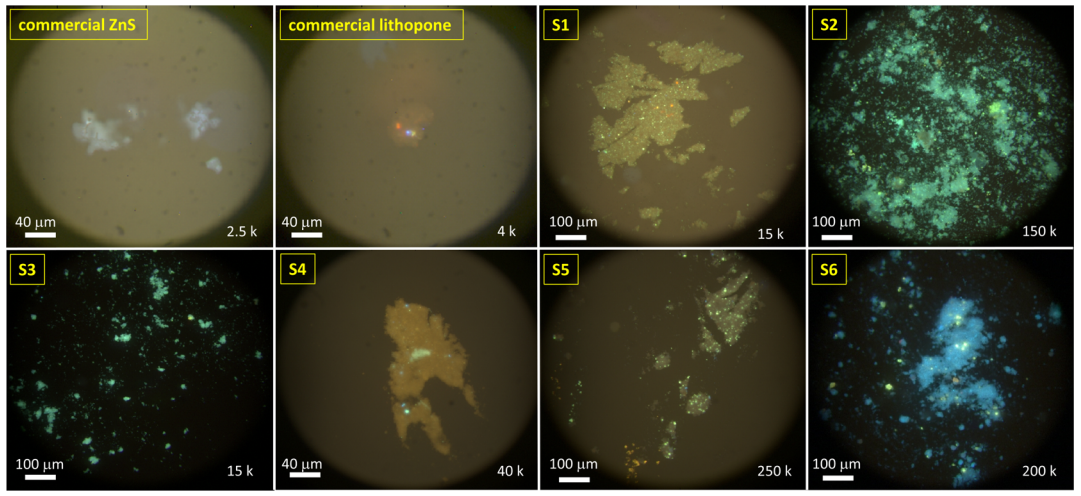

Figure 3. Reconstructed RGB images of the UV-induced PL emission for commercial samples of ZnS and lithopone and for the six historical lithopone samples (S1−6). At the bottom right of each image, the maximum PL intensity recorded is reported in counts. For commercial pigments, only a few luminescent centers have been detected, confirming the high purity of the material. Historical samples present a very bright luminescence, a uniform emitting matrix, and several localized centers of different size.

Table 2. Results of Analysis of Time-Resolved PL Decay Curves Fitted with a Multiexponential Model with a Maximum of Three Components, as Described in Ref 5, with Lifetime (τ_i) and Relative Weight ($A_i\tau_i$%) Values Given for Blue (BL), Green-Yellow (GL), and Orange (OL) Centers

	τ_1 (μs)	τ_2 (μs)	τ_3 (μs)	τ_1A_1 (%)	τ_2A_2 (%)	τ_3A_3 (%)	τ_{mean} (μs)	R^2
S2 (BL)	0.10	0.93	7.51	7.0	25.1	67.9	5.34	0.999
S2 (OL)	0.07	0.78	6.92	14.5	26.7	58.8	4.29	0.997
S4 (BL)	0.02	0.48	5.44	14.7	29.9	55.4	3.16	0.993
S4 (OL)	0.01	0.45	5.47	28.7	29.3	42.0	2.43	0.993
S5 (BL)	0.09	0.85	6.56	14.7	25.7	59.6	4.14	0.994
S5 (GL)	0.03	0.33	5.03	56.8	23.4	19.8	1.09	0.987
S5 (OL)	0.01	0.42	4.27	27.9	28.8	43.4	1.98	0.995
S6 (BL)	0.11	0.77	6.90	7.0	23.3	69.7	5.00	0.998
S6 (GL)	0.05	0.40	5.89	11.8	23.0	65.1	3.93	0.997
S6 (OL)	0.06	0.43	5.97	12.2	24.4	63.4	3.89	0.996

summarized in Table 2: PL decay curves are multiexponential in nature; all the samples are characterized by the presence of long-lived luminescent centers with an effective emission on the order of microseconds; the longest effective lifetime is always associated with the blue centers. The same trend was observed for all the samples (data not shown).

A detailed analysis of the emission from two representative samples, S5 and S6, is shown in Figures 4 and 5, with reconstructed RGB maps of the color of the emission, the emission lifetime map, PL spectra, and mean decay profiles of clustered emitting centers. In sample S5 (Figure 4), blue centers show effective lifetime τ_{mean} = 4.14 μs, green centers have τ_{mean} = 1.09 μs, and orange centers have τ_{mean} = 1.98 μs. The same analysis for sample S6 (Figure 5) highlights a blue luminescent matrix (τ_{mean} = 4.57 μs), blue emitting localized centers (τ_{mean} = 5.00 μs), green-yellow emitting centers (τ_{mean} = 3.93 μs), and a small cluster of orange luminescent inclusions (τ_{mean} = 3.89 μs). In sample S2, BL with the longest measured lifetime (τ_{mean} = 5.34 μs) and OL (τ_{mean} = 4.29 μs) emitting centers are detected, while in sample S4 BL (τ_{mean} = 3.16 μs) and OL (τ_{mean} = 2.43 μs) are identified. For these two samples, the analysis of the decay kinetics of the few green-yellow emitting centers gave inconsistent results, suggesting that more centers emitting at different wavelengths are superimposed, and we are unable to resolve them with our instrument. The presence of multiple superimposed centers was also found for sample S1.

EPR spectra registered from all historical samples exhibit a small peak at g = 4.3, a broad signal around g = 2.2, and a resolved hyper-fine pattern centered at g = 2 (shown in Figure 6a for sample S3). Figure 6b displays a highlight for the g = 2 region of the EPR spectrum for two representative samples (S1 and S3). A detailed discussion of the EPR results is provided below.

DISCUSSION OF RESULTS

Results obtained with PL and EPR can be explained by considering the historical synthesis of lithopone which involved the mixing of a solution of barium sulfide and zinc sulfate; the resulting coprecipitate of zinc sulfide and barium sulfate was then filtered, washed, and dried. Coprecipitation of the same amount of reagents is described by the following formula: $ZnSO_4 + BaS \rightarrow ZnS + BaSO_4$, yielding a product that is 29.4 wt % ZnS and 70.6 wt % $BaSO_4$.[20] This precipitate, generally referred to as crude lithopone, was then calcined at temperatures ranging from 600 to 900 °C and subsequently wet milled, filtered, and dried. The quality of the final lithopone depended essentially on two factors: the amount of ZnS with respect to that of $BaSO_4$[3] and the care exercised in the preparation of the two soluble salts, BaS and $ZnSO_4$, which

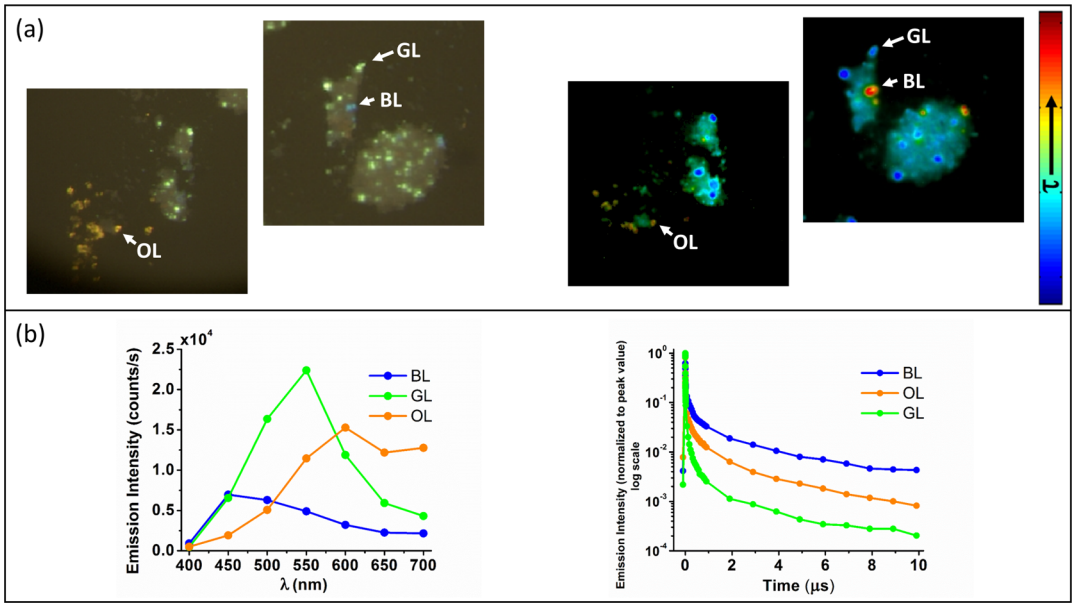

Figure 4. (a) RGB color maps of the PL emission for two selected areas of sample S5 (left) and lifetime maps of the same areas following monoexponential decay data fitting, shown in false color (right). RGB maps highlight the presence of small localized emitting centers giving rise to blue (BL), green-yellow (GL), and orange (OL) luminescence. Lifetime maps indicate that blue centers are the longest-living ones, followed by OL and GL. (b) PL spectra (left) and decay curves (right) recorded for the same sample in the areas labeled as BL, GL, and OL. The microsecond-decay kinetic behavior suggests that traps are responsible for the emitting centers.

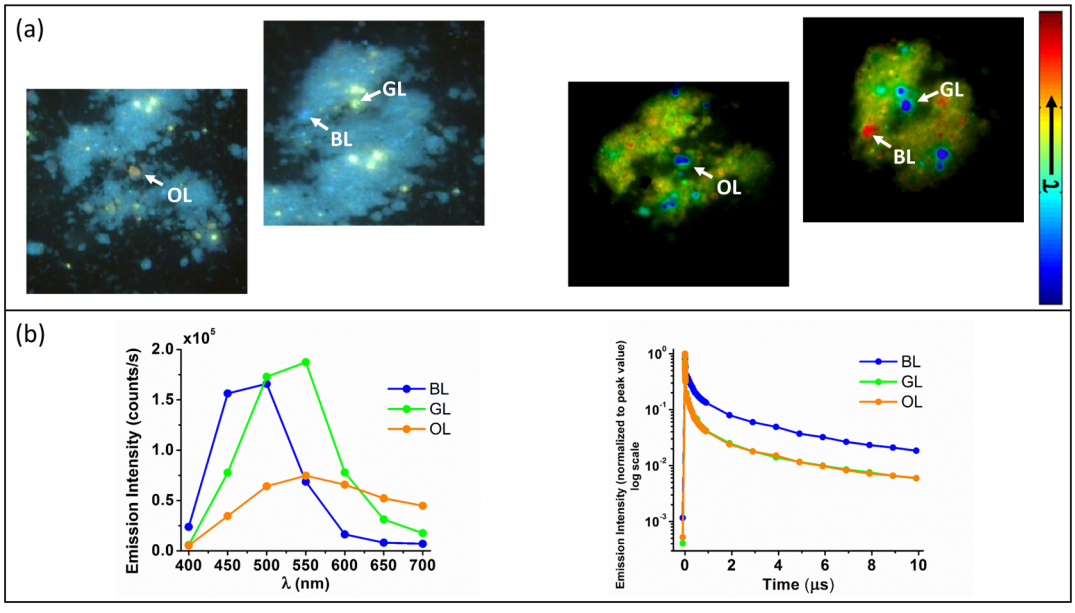

Figure 5. (a) RGB color maps of the PL emission for two selected areas of sample S6 (left) and lifetime maps of the same areas following monoexponential decay data fitting, shown in false color (right). These maps confirm the trend already observed for sample S5 in Figure 4: BL has a longer lifetime than GL and OL. (b) PL spectra (left) and decay curves (right) recorded for sample S6 in the areas labeled as BL, GL, and OL.

were prepared in the lithopone factory. $ZnSO_4$ was obtained by reprocessing zinc containing waste materials or directly from zinc ore. The most common ore employed was sphalaerite (historically known as zinc blende), a cubic resinous zinc iron sulfide mineral of composition (Zn,Fe)S.[21] Sphalerite is nearly always found with aluminum (Al) resulting from acidic weathering of rock and sulfide minerals, including salts of Mn, Cu, Ag, Cd, and Pb, resulting from mine drainage activity.[22] In order to obtain $ZnSO_4$, the zinc source material was leached in sulfuric acid, and other metallic impurities were precipitated as insoluble sulfides. The solution obtained was then filtered, washed, dried, and pulverized. Due to the impurity of the Zn sources and variability in the preparation of solutions, different metal impurities may have been introduced during various steps of lithopone synthesis.

Blue luminescence (BL) centers observed in lithopone samples can be attributed to interstitial Ag and Cu or to intrinsic ZnS defects. Ag substitutes Zn in the matrix and acts as an electron acceptor center, giving rise to an emission ranging from 420 to 440 nm depending on the presence of coactivators like Al (which usually causes a red-shift of the luminescence[17]). Cu forms two types of acceptor centers in ZnS matrix, and the

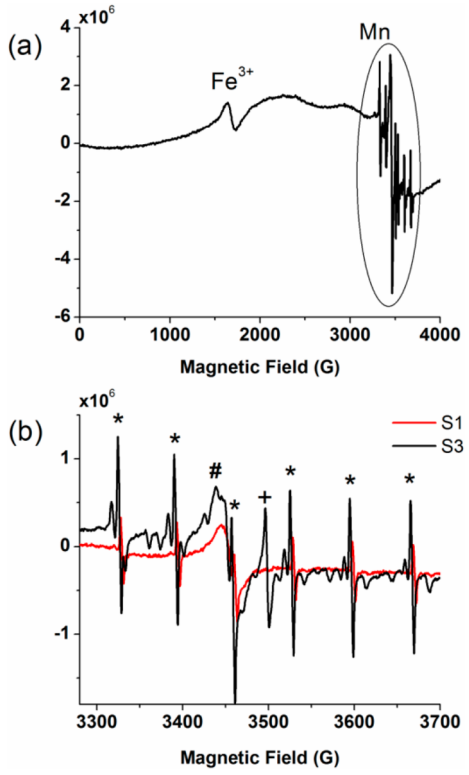

Figure 6. (a) EPR spectrum for sample S3. The Fe^{3+} signal with $3d^5$ electron configuration is observed at about $g = 4.3$. At about $g = 2$, a broad background signal is attributed to Mn ions in clusters. (b) Mn_{Zn}^{2+} hyperfine structure for samples S1 and S3 (the six peaks have been marked with asterisks): both the spectra are characterized by a system of lines surrounding each of the sextet sites, ascribable to crystal field effects small enough to be treated as perturbations. Organic radicals are also observed ($g = 2.009$, #) and ZnS defects ($g = 2.002$, +).

emission wavelength closely depends on the Cu-doped concentration:[13] the blue-Cu luminescence (BL) peaked at 472 nm is formed by positively charged interstitial Cu^+ ions [Cu_i^+]; Cu_i^+ centers trap electrons from the conduction band, which immediately recombine with free holes nonradiatively. Since the diffusion of Cu into the ZnS matrix is difficult, formation of interstitial Cu_i^+ centers can occur only with an excess of Cu doping. The so-called self-activated emission from crystals of ZnS, ascribed to the presence of intrinsic defects, also gives rise to blue luminescence.[7,8] A green-Cu luminescence (GL) peaked at 520 nm is formed by Cu substitutionally sitting at the Zn^{2+} site [Cu_{Zn}^{2+}] acting as a recombination center for electrons from either conduction band or shallow donor sites (e.g., S vacancies). Green Cu emission can be quenched when the concentration of Cu impurities increases beyond a certain limit, indicated as 3.5×10^{-4} mol %,[10] which promotes the blue Cu_i^+ luminescence. Therefore, the ratio between these two peaks may be a good indicator of the concentration of Cu doping. Orange luminescence (OL) arises from the incorporation of traces of Mn^{2+} in the crystal lattice and is peaked at around 580 nm.[10] The mechanism for the orange luminescence from Mn^{2+} doped ZnS is similar to that of Cu_{Zn}^{2+}, but in this case, Mn^{2+} acts as an isoelectronic dopant that substitutes at the Zn valence sites and acts as an attracting site for holes [Mn_{Zn}^{2+}] which therefore recombine with conduction band electrons or electrons in shallow donor sites.

PL properties show a complex behavior that reflects the great heterogeneity (different impurities and concentrations), confirmed by the multiexponential behavior of the luminescence decays. Few studies address the analysis of the dynamics of doped ZnS materials, and most highlight how differences in lattice structure are responsible for marked differences in kinetic properties: Lisensky et al.[23] modeled the dynamics of Cu-doped phosphors as a second-order equation, consistent with the recombination of equal populations of holes and electrons. Jayanthi et al.[12] measured the time-resolved decay of PL for undoped ZnS and ZnS/Cu nanoparticles, suggesting that, beneath the band gap excitation, carrier dynamics involves band to band excitation, trapping at sulfur vacancies, recombination at valence band or Cu level, and conduction band to Zn valence acceptor centers. Chen et al.[17] studied the role of codoping in the variation of the decay constant in Cu-doped ZnS phosphors. Due to the large range of applications of doped ZnS, its kinetic properties can be tuned from a microsecond up to several minutes; therefore, a comparison of time constants reported in this work with literature is not straightforward.

As a general feature, we can affirm that the type and concentration of dopants, as well as the local environment of an activator center, play a key role in determining the optical properties of the luminescence of lithopone, such as the intensity of the transitions and the energy at which the transitions occur. In addition, the environment of the activator may strongly affect the radiative decay time and the nature of the de-excitation mechanism.

EPR spectroscopy provides information on some of the structural and dynamic phenomena of lithopone samples and gives insights into impurities that influence their PL properties. The narrow peak at $g = 4.3$ (Figure 6a) arises from high spin $S = 5/2$ Fe^{3+} species; this peak is constant in all samples, and the concentration of Fe^{3+} can be considered similar for all samples. Fe is a common contaminant associated with spharelite with Fe^{2+} substitution for cation lattice Zn sites.[24] The presence of the Fe^{3+} state rather than Fe^{2+} might therefore be due to oxidation of spharelite [$Zn(S,Fe) + 2O_2 \rightarrow Zn(S,Fe)O_4$] during the grinding process of the mineral.[25] The broad line around $g = 2.2$, observed for all samples, can be ascribed to the presence of trace Cu_{Zn}^{2+}, which was predicted by PL analysis as a justification for the GL. At around $g = 2$, a broad signal superposed over hyperfine structure is consistent with the presence of Mn as a cluster and Mn^{2+} substituting Zn^{2+} sites, which is a reasonable explanation for the OL.[26] Figure 6b highlights that this signal, consisting of a complex of six sharp lines, identified as hyperfine structure Mn^{2+}, is due to the interaction of electron spin of Mn_{Zn}^{2+} with its nuclear spin $I = 5/2$. The spectrum further contains a system of lines between each component of the sextet, identified as the so-called forbidden transitions coming from the zero field splitting interactions, when the nuclear spin changes simultaneously with the orientation of the electron spin, due to high spin state of Mn^{2+} species.[26,27] The other two components, respectively centered at $g = 2.009$ and $g = 2.002$, can be attributed to the presence of organic radicals and ZnS defects,[28] which might be partially responsible for the blue luminescence detected in historical samples, which could be ascribed to the self-activated emission from ZnS crystals.[7,8]

CONCLUSIONS

Laboratory analyses on six historical luminescent lithopone samples revealed the presence of several emitting centers associated with metal ion impurities unintentionally introduced during the pigment synthesis. PL microscopic imaging revealed the presence of centers emitting at different wavelengths in the visible region, of different color and intensity from blue to red.

The combination of spatial and temporal PL microscopic imaging enabled the identification and qualitative characterization of luminescent lithopone impurities, while EPR allowed a more complete description of the chemical composition of the material. The EPR results confirm the presence of Cu_{Zn}^{2+} and Mn_{Zn}^{2+} ions, acting as impurities in all the historical samples, whereas Ag traces could not be detected. Further, the EPR results indicate the presence of Fe as a constituent of the ZnS mineral ores.

A complete understanding of the PL emission mechanisms in this material is not straightforward and would require the determination of the concentration of impurities and the ratio between different impurities. In the future, such information could be achieved via inductively coupled plasma mass spectrometry (ICPMS) or secondary ion mass spectrometry (SIMS). Nevertheless, these techniques require the destruction of sample which was not possible in our study due to the limited amount of available material. Furthermore, to determine the concentration of impurities through ICPMS, calibration standards would be required.

EPR data complement the analysis of the defect luminescence mechanism in lithopone without any sample destruction. This work demonstrates that, in the future, the investigation of the microenvironmental complexity of painting materials could benefit from the use of EPR imaging over conventional EPR techniques: indeed, visualizing the spatial distribution of paramagnetic centers and their physical and chemical properties could provide absolute and direct quantitative comparison with luminescence imaging results. Moreover, further complementary mapping techniques would help to better characterize the pigment and its impurities, as μ-Raman and synchrotron-based μ-XRF imaging.

The multianalytical approach described in this work was designed to answer specific research questions about the optical properties of lithopone. In particular, in the historical lithopone samples studied, an intense PL emission is attributed to a synthesis process developed within a specific period and geographical area. The analysis of further historical samples of this pigment could help in understanding a possible correlation between these luminescence properties and sources and production methods. The results obtained encourage further exploration of the same protocol for the study of the intrinsic heterogeneity of other painting materials. Moreover, the information gained through this laboratory-based protocol can help in the future in the interpretation of results obtainable by means of in situ, nondestructive investigation of the luminescence properties of real paintings.

ASSOCIATED CONTENT

Supporting Information

Scanning electron microscope (SEM) images for all the samples shown in this work. The Supporting Information is available free of charge on the ACS Publications websit0.

AUTHOR INFORMATION

Corresponding Author

*E-mail: sara.bellei@polimi.it. Fax: +39 02 23996126.

Present Address

[‖]A.C.: Department of Scientific Research, The Metropolitan Museum of Art, 1000 Fifth Avenue, New York, USA.

Funding

Research was partially funded by the Italian Ministry of Education, Universities and Research within the framework of the JPI Cultural Heritage – JHEP Pilot call through the LeadART project "Induced decay and aging mechanisms in paintings: focus on interactions between lead and zinc white and organic material"; within the Future in Research 2012 program through the FUTURAHMA project "From Futurism to Classicism (1910–1922). Research, Art History and Materials Analysis"; and through the Bilateral Project between Italy and The United States of America, funded by the Italian Ministry for Foreign Affairs and International Cooperation.

Notes

The authors declare no competing financial interest.

ACKNOWLEDGMENTS

The authors gratefully acknowledge Joe Barabe of McCrone Associates for providing all the historical lithopone samples discussed in this artwork and Dr. Maria Cristina Mozzati (University of Pavia) for her contribution in the interpretation of EPR data.

REFERENCES

(1) Goshorn, J. H.; Black, C. K. *Ind. Eng. Chem.* **1929**, *21*, 348–349.
(2) Jantsch, G.; Wolski, P. US Patent 1,693,902, 1928.
(3) Capua, R. *J. Am. Inst. Conserv.* **2014**, *53*, 75–88.
(4) Boselli, L.; Ciattini, S.; Galeotti, M.; Lanfranchi, M. R.; Lofrumento, C.; Picollo, M.; Zoppi, A. *e-Preservation Sci.* **2009**, *6*, 38–42.
(5) Comelli, D.; Nevin, A.; Brambilla, A.; Osticioli, I.; Valentini, G.; Toniolo, L.; Fratelli, M.; Cubeddu, R. *Appl. Phys. A: Mater. Sci. Process.* **2012**, *106*, 25–34.
(6) Fang, X.; Zhai, T.; Gautam, U. K.; Li, L.; Wu, L.; Bando, Y.; Golberg, D. *Prog. Mater. Sci.* **2011**, *56*, 175–287.
(7) Denzler, D.; Olschewski, M.; Sattler, K. *J. Appl. Phys.* **1998**, *84*, 2841.
(8) Kurbatov, D.; Opanasyuk, A.; Kshnyakina, S.; Myelnik, V.; Nesprava, V. *Rom. Rep. Phys.* **2010**, *55*, 213–219.
(9) Cao, J.; Yang, J.; Zhang, Y.; Yang, L.; Wang, Y.; Wei, M.; Liu, Y. *J. Alloys Compd.* **2009**, *486*, 890–894.
(10) Ben, P. V.; Tue, P. T. *J. Sci. Math.* **2008**, *24*, 181–187.
(11) Chung, H. V.; Huy, P. T.; An, T. T.; Chien, N. D. *J. Korean Phys. Soc.* **2008**, *52*, 1562–1565.
(12) Jayanthi, K.; Chawla, S.; Chander, H.; Haranath, D. *Cryst. Res. Technol.* **2007**, *42*, 976–982.
(13) Manzoor, K.; Vadera, S. R.; Kumar, N.; Kutty, T. R. N. *Mater. Chem. Phys.* **2003**, *82*, 718–725.
(14) Hao, E.; Sun, Y.; Yang, B.; Zhang, X.; Liu, J.; Shen, J. *J. Colloid Interface Sci.* **1998**, *204*, 369–373.
(15) Murugadoss, A.; Chattopadhyay, A. *Bull. Mater. Sci.* **2008**, *31*, 533–539.
(16) Kawai, H.; Kuboniwa, S.; Hoshina, T. *Jpn. J. Appl. Phys.* **1974**, *13*, 1593–1603.
(17) Chen, Y. Y.; Duh, J. G.; Chiou, B. S.; Peng, C. G. *Thin Solid Films* **2001**, *392*, 50–55.
(18) Cesaratto, A.; D'Andrea, C.; Nevin, A.; Valentini, G.; Tassone, F.; Alberti, R.; Frizzi, T.; Comelli, D. *Anal. Methods* **2014**, *6*, 130.

(19) Brambilla, A.; Osticioli, I.; Nevin, A.; Comelli, D.; D'Andrea, C.; Lofrumento, C.; Valentini, G.; Cubeddu, R. *Rev. Sci. Instrum.* **2011**, *82*, 063109.
(20) Völz, H. G.; Kischkewitz, J.; Woditsch, P.; Westerhaus, A.; Griebler, W.-D.; De Liedekerke, M.; Buxbaum, G.; Printzen, H.; Mansmann, M.; Räde, D.; Trenczek, G.; Wilhelm, V.; Schwarz, S.; Wienand, H.; Adel, J.; Adrian, G.; Brandt, K.; Cork, W. B.; Winkeler, H.; Mayer, W.; Schneider, K.; Leitner, L.; Kathrein, H.; Schwab, E.; Jakusch, H.; Ohlinger, M.; Veitch, R.; Etzrodt, G.; Pfaff, G.; Franz, K.-D.; Emmert, R.; Nitta, K.; Besold, R.; Gaedcke, H. In *Ullmann's Encyclopedia of Industrial Chemistry*; Wiley-VCH Verlag GmbH & Co. KGaA: New York, 2000.
(21) Balabin, A. I.; Sack, R. O. *Mineral. Mag.* **2000**, *64*, 923−943.
(22) Cook, N. J.; Ciobanu, C. L.; Pring, A.; Skinner, W.; Shimizu, M.; Danyushevsky, L.; Saini-Eidukat, B.; Melcher, F. *Geochim. Cosmochim. Acta* **2009**, *73*, 4761−4791.
(23) Lisensky, G. C.; Patel, M. N.; Reich, M. L. *J. Chem. Educ.* **1996**, *73*, 1048.
(24) Hoffmann, H.; Heitz, R.; Broser, I. *Phys. Rev. B* **1990**, *41*, 5806−5816.
(25) Steger, H. F.; Desjardins, L. E. *Can. Mineral.* **1980**, *18*, 365−372.
(26) Liu, J.; Liu, C.; Zheng, Y.; Li, D.; Xu, W.; Yu, J. *J. Phys.: Condens. Matter* **1999**, *11*, 5377−5384.
(27) Stefan, M.; Nistor, S. V.; Ghica, D.; Mateescu, C. D.; Nikl, M.; Kucerkova, R. *Phys. Rev. B: Condens. Matter Mater. Phys.* **2011**, *83*, 1−11.
(28) Murase, N.; Jagannathan, R.; Kanematsu, Y.; Watanabe, M.; Kurita, A.; Hirata, K.; Yazawa, T.; Kushida, T. *J. Phys. Chem. B* **1999**, *103*, 754−760.